New type of Weyl semimetal with quadratic double Weyl fermions

Shin-Ming Huang[a,b,1], Su-Yang Xu[c,1,2], Ilya Belopolski[c,1], Chi-Cheng Lee[a,b], Guoqing Chang[a,b], Tay-Rong Chang[c,d,e], BaoKai Wang[a,b,f], Nasser Alidoust[c], Guang Bian[c], Madhab Neupane[c], Daniel Sanchez[c], Hao Zheng[c], Horng-Tay Jeng[d,g], Arun Bansil[f], Titus Neupert[h], Hsin Lin[a,b,2], and M. Zahid Hasan[c,2]

[a]Centre for Advanced 2D Materials and Graphene Research Centre, National University of Singapore, Singapore 117546; [b]Department of Physics, National University of Singapore, Singapore 117542; [c]Joseph Henry Laboratory, Department of Physics, Princeton University, Princeton, NJ 08544; [d]Department of Physics, National Tsing Hua University, Hsinchu 30013, Taiwan; [e]Laboratory for Topological Quantum Matter and Spectroscopy (B7), Department of Physics, Princeton University, Princeton, NJ 08544; [f]Department of Physics, Northeastern University, Boston, MA 02115; [g]Institute of Physics, Academia Sinica, Taipei 11529, Taiwan; and [h]Princeton Center for Theoretical Science, Princeton University, Princeton, NJ 08544

Edited by Philip Kim, Harvard University, Cambridge, MA, and accepted by the Editorial Board December 6, 2015 (received for review July 23, 2015)

Weyl semimetals have attracted worldwide attention due to their wide range of exotic properties predicted in theories. The experimental realization had remained elusive for a long time despite much effort. Very recently, the first Weyl semimetal has been discovered in an inversion-breaking, stoichiometric solid TaAs. So far, the TaAs class remains the only Weyl semimetal available in real materials. To facilitate the transition of Weyl semimetals from the realm of purely theoretical interest to the realm of experimental studies and device applications, it is of crucial importance to identify other robust candidates that are experimentally feasible to be realized. In this paper, we propose such a Weyl semimetal candidate in an inversion-breaking, stoichiometric compound strontium silicide, $SrSi_2$, with many new and novel properties that are distinct from TaAs. We show that $SrSi_2$ is a Weyl semimetal even without spin–orbit coupling and that, after the inclusion of spin–orbit coupling, two Weyl fermions stick together forming an exotic double Weyl fermion with quadratic dispersions and a higher chiral charge of ± 2. Moreover, we find that the Weyl nodes with opposite charges are located at different energies due to the absence of mirror symmetry in $SrSi_2$, paving the way for the realization of the chiral magnetic effect. Our systematic results not only identify a much-needed robust Weyl semimetal candidate but also open the door to new topological Weyl physics that is not possible in TaAs.

topological insulator | Weyl fermion | Fermi arc | chiral magnetic effect

Analogous to graphene and the 3D topological insulator, Weyl semimetals are believed to open the next era in condensed matter physics (1–8). A Weyl semimetal represents an elegant example of the correspondence between condensed matter and high-energy physics because its low-energy excitations, the Weyl fermions, are massless particles that have played an important role in quantum field theory and the standard model but have not been observed as a fundamental particle in nature. A Weyl semimetal is also a topologically nontrivial metallic phase of matter extending the classification of topological phases beyond insulators (3–6). The nontrivial topological nature guarantees the existence of exotic Fermi arc electron states on the surface of a Weyl semimetal. In contrast with a topological insulator where the bulk is gapped and only the Dirac cones on its surfaces are of interest, in a Weyl semimetal, both the Weyl fermions in the bulk and the Fermi arcs on the surface are fundamentally new and are expected to give rise to a wide range of exotic phenomena (9–22).

For many years, research on Weyl semimetals has been held back due to the lack of experimentally feasible candidate materials. Early theoretical proposals require either magnetic ordering in sufficiently large domains (3, 23–26) or fine-tuning of the chemical composition to within 5% in an alloy (23, 25–27), which proved demanding in real experiments. Recently, our group and a concurrent group successfully proposed the first, to our knowledge, experimentally feasible Weyl semimetal candidate in TaAs material class (28, 29). The key is that TaAs is an inversion symmetry-breaking, stoichiometric, single-crystalline material, which does not depend on any magnetic ordering or fine-tuning. Shortly after the prediction, the first, to our knowledge, Weyl semimetal state was experimentally discovered in TaAs via photoemission spectroscopy (30, 31). Later, other photoemission works confirmed the discovery in several members of the TaAs material class (32–35).

In this paper, we propose a new type of Weyl semimetal in an inversion-breaking, stoichiometric compound strontium silicide, $SrSi_2$. Our first-principles band structure calculations show that $SrSi_2$ is already a Weyl semimetal even in the absence of spin–orbit coupling. After including spin–orbit coupling, two linearly dispersive Weyl fermions with the same chiral charge are bounded together, forming a quadratically dispersive Weyl fermion. We find that such a quadratically dispersive Weyl fermion exhibits a chiral charge of 2 (compared with 1 in the TaAs family). Furthermore, because $SrSi_2$ lacks both mirror and inversion symmetries, the Weyl nodes with opposite charges are located at different energies. This property may facilitate the realization of the chiral magnetic effect (10–14). This effect has attracted much theoretical interest, because it seems to violate basic results of band theory by suggesting that a Weyl semimetal can support dissipationless currents in equilibrium. Recent theoretical works have clarified the apparent contradiction (see ref. 15 and references therein and,

Significance

We predict a new Weyl semimetal candidate. This is critically needed for this rapidly developing field as TaAs is the only known Weyl semimetal in nature. We show that $SrSi_2$ has many new and novel properties not possible in TaAs. Our prediction provides a new route to studying the elusive Weyl fermion particles originally considered in high-energy physics by tabletop experiments.

Author contributions: S.-M.H., S.-Y.X., I.B., C.-C.L., G.C., T.-R.C., B.W., N.A., G.B., M.N., D.S., H.Z., H.-T.J., A.B., T.N., H.L., and M.Z.H. contributed to the intellectual contents of this work; preliminary material search and analysis were done by S.-Y.X. and I.B. with help from N.A., G.B., M.N., D.S., H.Z., and M.Z.H.; S.-Y.X. designed research; S.-M.H., C.-C.L., G.C., T.-R.C., B.W., H.-T.J., A.B., T.N., and H.L. performed theoretical analysis and computations; S.-M.H., S.-Y.X., C.-C.L., G.C., B.W., N.A., G.B., M.N., D.S., H.Z., H.-T.J., A.B., T.N., H.L., and M.Z.H. analyzed data; S.-M.H., S.-Y.X., I.B., T.N., H.L., and M.Z.H. wrote the paper; H.L. supervised the theoretical part of the work; and M.Z.H. was responsible for the overall physics and research direction, planning, and integration among different research units.

The authors declare no conflict of interest.

This article is a PNAS Direct Submission. P.K. is a guest editor invited by the Editorial Board.

Freely available online through the PNAS open access option.

[1]S.-M.H., S.-Y.X., and I.B. contributed equally to this work.

[2]To whom correspondence may be addressed. Email: suyangxu@princeton.edu, nilnish@gmail.com, or mzhasan@princeton.edu.

This article contains supporting information online at www.pnas.org/lookup/suppl/doi:10.1073/pnas.1514581113/-/DCSupplemental.

e.g., ref. 16). Our prediction of the Weyl semimetal state in $SrSi_2$ is of importance because it identifies a much-needed robust Weyl semimetal candidate, paves the way for realizing quadratically dispersive Weyl fermions with higher chiral charges, and allows one to test the theoretical debates of the chiral magnetic effect by direct experimental measurement of a real material.

Results

We computed electronic structures using the norm-conserving pseudopotentials as implemented in the OpenMX package within the generalized gradient approximation schemes (36). Experimental lattice constants were used (37). A $12\times12\times12$ Monkhorst–Pack k-point mesh was used in the computations. The spin–orbit effects were included self-consistently. For each Sr atom, three, two, two, and two optimized radial functions were allocated for the s, p, d, and f orbitals ($s3p2d2f2$), respectively, with a cutoff radius of 10 Bohr. For each Si atom, $d2p2d1$ was adopted with a cutoff radius of 7 Bohr. A regular mesh of 600 Ry in real space was used for the numerical integrations and for the solution of the Poisson equation. To calculate the surface electronic structures, we constructed a first-principles tight-binding model Hamiltonian. The tight-binding model matrix elements are calculated by projecting onto the Wannier orbitals (38). We use Sr s and d and Si s and p orbitals without performing the procedure for maximizing localization.

$SrSi_2$ crystallizes in a simple cubic lattice system (37, 39, 40). The lattice constant is $a=6.563$ Å and the space group is $P4_332$ (#212). As seen in Fig. 1*A*, the crystal lacks inversion and mirror symmetries. The bulk and (001) surface high-symmetry points are noted in Fig. 1*B*, where the centers of the square faces are the X,Y,Z points (X,Y,Z are equivalent), the centers of the edges are the M points, and the corners of the cube are the R points.

We understand the electronic properties of $SrSi_2$ at a qualitative level based on the ionic model. The electronic configuration of Sr is $4s^2$ whereas the electronic configuration of Si is $3s^23p^2$. Each Sr atom has a strong tendency to give out two electrons to achieve a full shell configuration in an ionic compound, leading to an ionic state of Sr^{+2}. This means that, in $SrSi_2$, Si has an ionic state of Si^{-1}, which is different from the most common ionic state of Si, Si^{+4}, as in SiO_2. This situation resembles another well-known semimetal, Na_3Bi. In both compounds, an element that usually forms a positive ionic state (such as Si^{+4} or Bi^{+3}) in an ionic compound is forced to form a negative ionic state (such as Si^{-1} or Bi^{-3}). However, we emphasize that a key difference between $SrSi_2$ and Na_3Bi is that the $SrSi_2$ crystal breaks space-inversion symmetry. Based on the above picture, we expect that the valence electronic states mainly arise from the $3p$ orbitals of Si. Indeed, this is confirmed by our first-principles calculation results. Fig. 1*C* shows the calculated bulk band structure along high-symmetry directions in the absence of spin–orbit coupling. We observe a clear crossing between the bulk conduction and valence bands along the $\Gamma-X$ direction, which agrees with our expectation of $SrSi_2$ being a semimetal. Interestingly, we note that the band crossing does not enclose any high-symmetry or time-reversal invariant Kramers' points. In the vicinity of the crossings, the bands are found to disperse linearly along the $\Gamma-X$ direction as shown in Fig. 1*D*. The two crossings along $\Gamma-X$ without spin–orbit coupling are denoted as W1 and W2. In the presence of spin–orbit coupling, bands with the same rotation eigenvalues are gapped out whereas those with different rotation eigenvalues remain gapless as shown in Fig. 1 *E* and *F*. We denote the band crossings after the inclusion of spin–orbit coupling as W1′ and W2′.

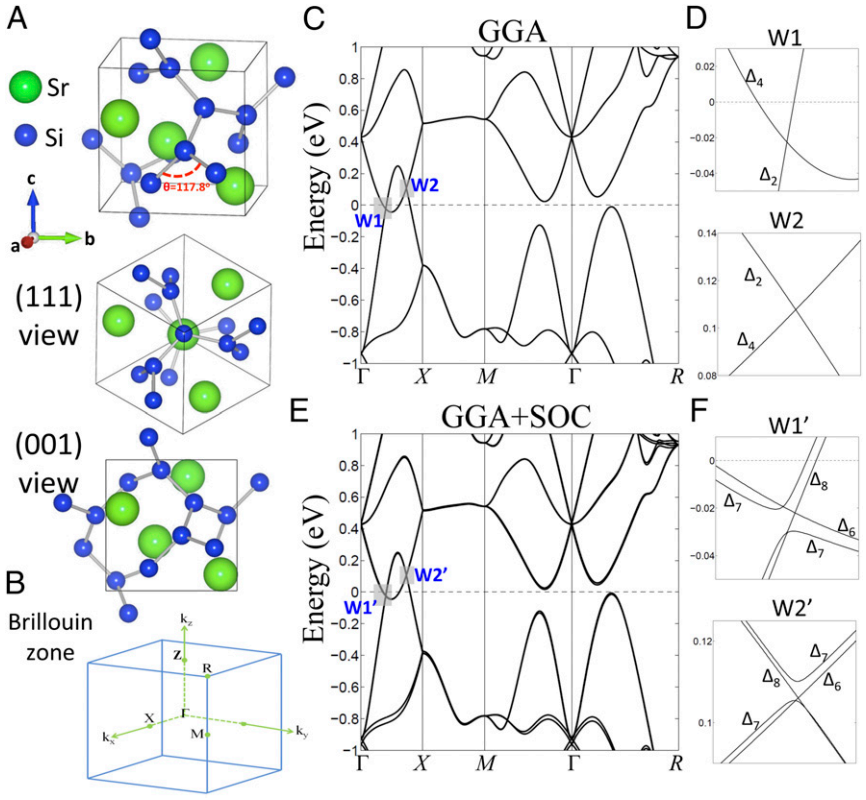

Fig. 1. Crystal and electronic structure of $SrSi_2$. (*A*) Crystal structure of $SrSi_2$. (*B*) Bulk BZ of $SrSi_2$ with the high-symmetry points noted. (*C*) First-principles band structure calculation without spin–orbit coupling. (*D*) Zoomed-in version of the band structure near the spinless Weyl nodes W1 and W2. (*E* and *F*) The same as *C* and *D* but with spin–orbit coupling. Upon the inclusion of spin–orbit coupling, bands with the same rotation eigenvalues are gapped out whereas those with different rotation eigenvalues remain gapless, forming Weyl nodes W1′ and W2′. Δ_i notes the representations of bands along the $\Gamma-X$ direction.

We systematically study the nature of the band crossings in Fig. 2. In the absence of spin–orbit coupling, our calculation shows that the bands disperse linearly along all three directions in the vicinity of each W1 or W2 (Fig. 2*D*). We have calculated the chiral charge associated with W1 and W2 by calculating the Berry flux through a closed surface that encloses a node. Our calculation shows that both W1 and W2 carry a nonzero chiral charge and that they have opposite charges. These calculations prove that they are Weyl nodes. Therefore, $SrSi_2$ is already a Weyl semimetal even without spin–orbit coupling. We have calculated the band structure throughout the first Brillouin zone (BZ). As shown in Fig. 2*A*, in total there are 60 Weyl nodes within the first BZ without spin–orbit coupling. These 60 Weyl nodes can be categorized into four groups. W1 and W2 are the Weyl nodes located on the Γ–$X(Y,Z)$ axes. W3 and W4 are located on the Γ–X–Y–M and Γ–Z–R–M planes (Fig. 2*B*).

We now consider the band structure with spin–orbit coupling. We note that each Weyl node without spin–orbit coupling should be considered as two degenerate Weyl nodes with the same chiral charge but with the opposite physical spins. In general, spin–orbit coupling is expected to lift the degeneracy of the physical spin due to the lack of inversion symmetry in $SrSi_2$. Each of the W3 (respectively, W4) (Fig. 2*C*) nodes splits into two Weyl nodes with the same chiral charge, W3′ and W3″ (W4′ and W4″), which are separated in momentum space. The nodes W1 and W2, in contrast, do not split, but their dispersion changes from linear to quadratic. Specifically, a W1′ cone on the k_x axis disperses quadratically along k_y and k_z directions whereas its dispersion along k_x remains linear (Fig. 2*E*). We have calculated the chiral charge associated with the quadratic Weyl nodes and our results reveal a chiral charge of ±2. Usually, the Weyl cones in a Weyl semimetal disperse linearly and have chiral charges of ±1. The existence of quadratically dispersive Weyl fermions is interesting in itself. Furthermore, recent theoretical studies have suggested that a quadratic band touching may lead to interesting non-Fermi liquid interaction effects because the long-range tail of the Coulomb repulsion is not screened (41–43).

We can understand how spin–orbit coupling turns the doubly degenerate linear W1 node into a quadratic node by examining the action of C_4 rotation symmetry on an effective $\boldsymbol{k}\cdot\boldsymbol{p}$ Hamiltonian. We note that all of the quadratically dispersive Weyl nodes are located on the k_x, k_y, and k_z axes which are the C_4 rotational axes of the crystal, suggesting that they are protected by the C_4 symmetry. Using the Pauli matrices σ_1, σ_2, σ_3 in spin space, C_4 rotations around the z axis are represented by $e^{-i\pi\sigma_3/4}$. We choose the same representation $e^{-i\pi\tau_3/4}$ acting on the orbital space Pauli matrices τ_1, τ_2, τ_3, that is, $R_{C_4}=e^{-i\pi\tau_3/4}\otimes e^{-i\pi\sigma_3/4}$. The doubly degenerate Weyl Hamiltonian that is C_4 invariant, i.e., that obeys $R_{C_4}H(k_x,k_y,k_z)R_{C_4}^{-1}=H(k_y,-k_x,k_z)$, in the absence of spin–orbit coupling is then given by

$$H=vk_x\tau_x+vk_y\tau_y+v'k_z\tau_z. \qquad [1]$$

With spin–orbit coupling, we can add three $\boldsymbol{k}$-independent terms to the Hamiltonian that commute with R_{C_4}: (*i*) $\tau_3\otimes\sigma_3$, (*ii*) $\tau_1\otimes\sigma_1+\tau_2\otimes\sigma_2$, and (*iii*) $\tau_2\otimes\sigma_1-\tau_1\otimes\sigma_2$. The first term separates the Weyl nodes along k_z, whereas either of the latter two generates the quadratic touching seen in our first-principles calculations. We conclude that the latter terms dominate in $SrSi_2$. More precisely, if we add Δ times the term (*ii*) to H, the two bands that touch are given by

$$\varepsilon_{k,k_z}=\pm\sqrt{v^2k^2+v'^2k_z^2+2\Delta\left(\Delta-\sqrt{v^2k^2+\Delta^2}\right)}, \qquad [2]$$

with $k=\sqrt{k_x^2+k_y^2}$. They disperse quadratically like $v^2k^2/2\Delta$ for $k_z=0$ and linearly like $v'k_z$ for $k=0$.

To test the symmetry protection of the quadratic touching, we apply a uniaxial pressure along the $\hat{z}$ direction (Fig. 3*A*),

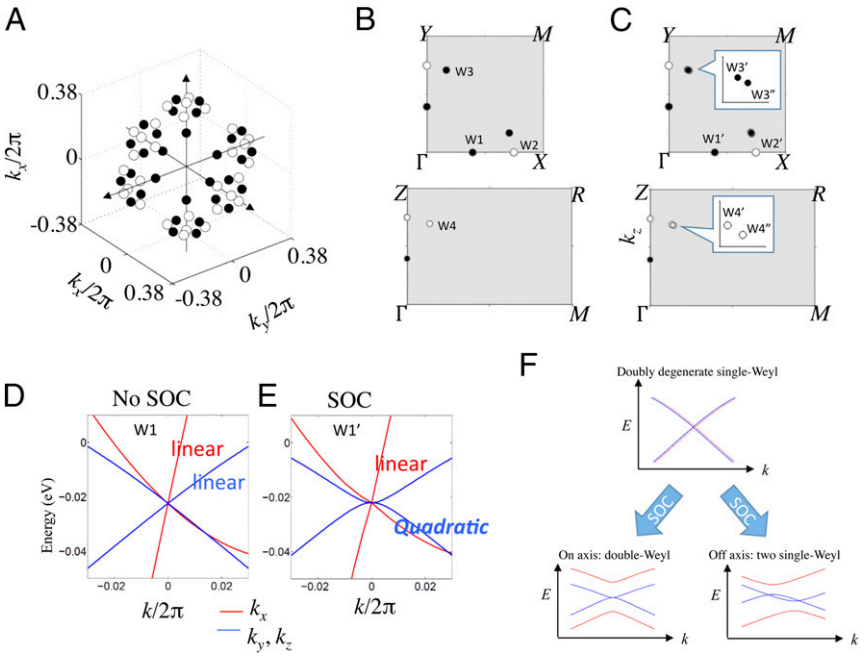

Fig. 2. Bulk Weyl nodes in $SrSi_2$. (*A*) Locations of the Weyl nodes within the first BZ without spin–orbit coupling. Colors of circles represent the signs of the chiral charge. (*B* and *C*) In the absence of spin–orbit coupling, the Weyl nodes can be categorized into four groups. W1 and W2 are located in the $\Gamma-X(Y,Z)$ direction. W3 and W4 are located on the $\Gamma-X-Y$ and the $\Gamma-Z-M$ planes. Please refer to Fig. 1*B* for the definition of these planes. In the presence of spin–orbit coupling, each W3 or W4 splits into two linearly dispersive (charge 1) Weyl nodes with the same chiral charge. Each W1or W2 becomes a quadratically dispersive (charge 2) Weyl node. We denote the Weyl nodes with extra primes (e.g., W1 becomes W1′) after including spin–orbit coupling. (*D* and *E*) Energy dispersions of a W1(W1′) Weyl cone with and without spin–orbit coupling. (*F*) Schematic illustration of the evolution of Weyl cones upon the inclusion of spin–orbit coupling.

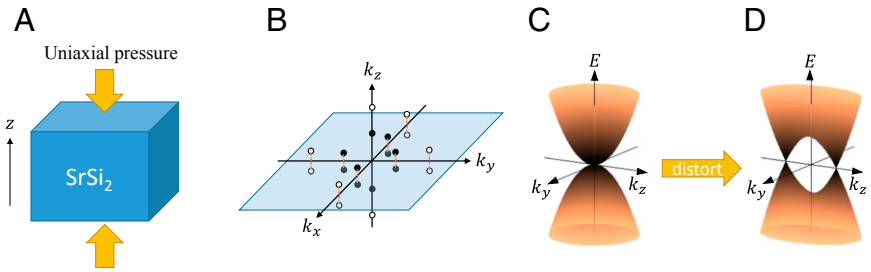

Fig. 3. Crystalline symmetry-protected quadratically dispersive Weyl nodes. (*A*) Uniaxial pressure along the $\hat{z}$ direction breaks the C_4 rotational symmetries along the k_x- and k_y axes. (*B*) Under this pressure, each quadratically dispersive Weyl node with a chiral charge of ±2 on the k_x or k_y axis splits into two linearly dispersive Weyl nodes with a chiral charge of ±1. (*C* and *D*) Schematic illustration of the evolution of a quadratically dispersive Weyl node on the k_x axis under crystalline symmetry breaking.

which breaks the C_4 symmetries along the k_x and k_y directions but preserves the C_4 symmetry along the k_z direction. Under such pressure, our calculations (Fig. 3*B*) show that each quadratically dispersive Weyl node located on the k_x (k_y) axis splits into two linearly dispersive Weyl nodes away from the axis. By contrast, the nodes on k_z remain intact. Previously, quadratically dispersive Weyl fermions were predicted in the Weyl semimetal candidate $HgCr_2Se_4$ (24, 44). However, the experimental realization of the Weyl semimetal state in $HgCr_2Se_4$ has been proven to be difficult, because there is no preferred magnetization axis in its cubic structure, which likely leads to the formation of many small ferromagnetic domains.

Besides the quadratically dispersive Weyl fermions, our calculations show another interesting property of $SrSi_2$. The Weyl nodes with opposite charges are located at different energies. We note that among all Weyl semimetal candidate materials, $SrSi_2$ is the first one, to our knowledge, to have this property. It arises from the lack of any mirror symmetry in the $SrSi_2$ crystal, because a mirror symmetry operation would reflect a Weyl node on one side of the mirror plane to a Weyl node with the opposite chiral charge at the same energy. Such a property is interesting because it enables the chiral magnetic effect (11–14). We propose that $SrSi_2$ provides an ideal material platform that allows one to test the chiral magnetic effect.

A key signature of a Weyl semimetal is the presence of Fermi arc surface states. We present calculations of the (001) surface states in Fig. 4. The projected Weyl nodes are denoted as black and white circles in Fig. 4*A*. The bigger circles correspond to the quadratic Weyl nodes with chiral charges of ±2 whereas the smaller ones correspond to the linear Weyl nodes with chiral charges of ±1. Our calculated surface Fermi surface shows the existence of Fermi arcs that terminate at the projections of the Weyl nodes. For example, the *k*-space region highlighted by the blue dotted box reveals two Fermi arcs terminating at the projection of a quadratically dispersive Weyl node (the black circle). This is consistent with its chiral charge of 2. The two Fermi arcs are close to each other in *k* space because the spin–orbit coupling is fairly weak in $SrSi_2$. We stress that because the W1 nodes are far separated in momentum space from any other Weyl node, topologically protected Fermi arcs stretch across a substantial portion of the surface BZ. This has to be contrasted with TaAs, where Weyl nodes of opposite chiral charge are rather close to one another.

We now study the energy dispersion of the surface states. The dispersion along cut 1 (the black dotted line in Fig. 4*A*) is shown in Fig. 4*B*. On each surface, there are four copropagating and two counterpropagating surface states. Therefore, the Chern number associated with the 2D *k* slice (cut 1) is 2. The Chern number associated with cut 2 (the green dotted line in Fig. 4*A*) must be 0 because it goes through the Kramers points $\overline{Y}$ $(0,\pi)$ and $\overline{M}$ (π,π). This result agrees with the total chiral charge, 2, which is enclosed by the surface formed by cut 1 and cut 2 in the bulk. (It encloses eight W4 nodes, eight W3 nodes, and one W2 node with the chiral charge +1, −1, and +2, respectively.)

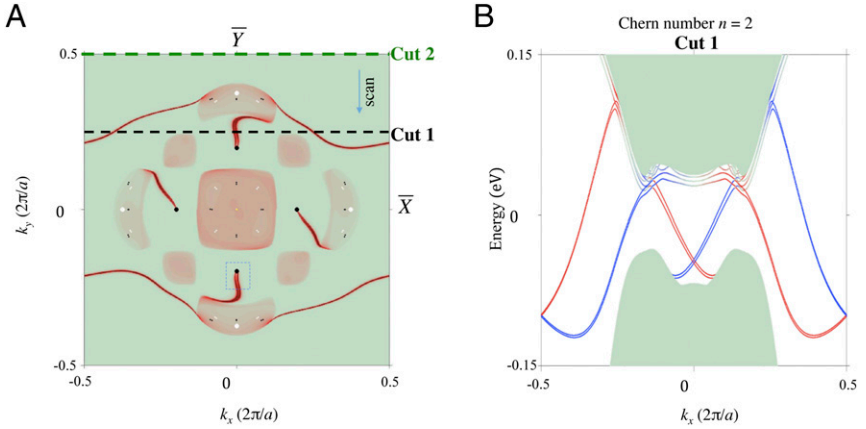

Fig. 4. Fermi arc surface states surface states on the (001) surface of $SrSi_2$. (*A*) Calculated surface-state Fermi surface of the (001) surface of $SrSi_2$. The sharp red lines show the surface states, the shaded areas show the surface projections of bulk bands, and the black and white circles show the projected Weyl nodes. The larger circles are the quadratically dispersive Weyl nodes with a chiral charge of ±2, whereas the smaller ones are the linearly dispersive Weyl nodes with a chiral charge of ±1. Cut 1 and cut 2 are two line-cuts through the surface BZ along the k_x direction. They correspond to the projection of two 2D k_x, k_z slices in the bulk BZ. (*B*) *E*-*k* dispersion along cut 1, noted by the dotted line in *A*. The red lines represent surface states from the top surface whereas the blue ones are from the bottom surface. The shaded areas are the projection of the bulk bands.

In summary, we have presented first-principles band structure calculations that predict $SrSi_2$ as a Weyl semimetal candidate. Similar to TaAs, $SrSi_2$ is an inversion-breaking, stoichiometric single crystal, which highlights its experimental feasibility. Our prediction here is reliable and robust, to the same extent as our previous predictions of the topological insulator state in Bi_2Se_3 (45) and topological Weyl semimetal states TaAs (28), both of which have now been experimentally realized (30, 45). We note that the Weyl semimetal state can be further stabilized by applying external pressure to compress the lattice. Our results identify a much-needed robust Weyl semimetal candidate. The predicted Weyl semimetal state in $SrSi_2$ also offers many distinctive properties not present in the TaAs family of materials.

ACKNOWLEDGMENTS. H.-T.J. thanks the National Center for High-Performance Computing, Computer and Information Network Center National Taiwan University, and National Center for Theoretical Sciences, Taiwan, for technical support. Work at Princeton University was supported by the US Department of Energy (DOE), Office of Science, Basic Energy Sciences (BES) under DE-FG-02-05ER46200. Work at the National University of Singapore was supported by the National Research Foundation (NRF), Prime Minister's Office, Singapore, under its NRF fellowship (NRF Award NRF-NRFF2013-03). T.-R.C. and H.-T.J. were supported by the National Science Council, Taiwan. The work at Northeastern University was supported by the US DOE/BES Grant DE-FG02-07ER46352, and benefited from Northeastern University's Advanced Scientific Computation Center (ASCC) and the National Energy Research Scientific Computing Center (NERSC) supercomputing center through DOE Grant DE-AC02-05CH11231. S.-M.H., G.C., T.-R.C., and H.L.'s visits to Princeton University are funded by the Gordon and Betty Moore Foundation's Emergent Phenomena in Quantum Systems (EPiQS) Initiative through Grant GBMF4547 (to M.Z.H.).

1. Weyl H (1929) Elektron und gravitation. I. *Z Phys* 56(5):330–352.
2. Balents L (1929) Weyl electrons kiss. *Physics* 4:36.
3. Wan XG, Turner AM, Vishwanath A, Savrasov S (2011) Topological semimetal and fermi-arc surface states in the electronic structure of pyrochlore iridates. *Phys Rev B* 83(20):205101.
4. Murakami S (2007) Phase transition between the quantum spin Hall and insulator phases in 3D: Emergence of a topological gapless phase. *New J Phys* 9(9):356.
5. Hasan MZ, Xu S-Y, Neupane M (2015) Topological insulators, topological crystalline insulators, topological Kondo insulators, and topological semimetals. *Topological Insulators: Fundamentals and Perspectives*, eds Ortmann F, Roche S, Valenzuela SO (John Wiley & Sons, New York).
6. Turner AM, Vishwanath A (2013) Beyond band insulators: Topology of semi-metals and interacting phases. arXiv:1301.0330v1.
7. Hasan M, Kane CL (2010) Colloquium: Topological insulators. *Rev Mod Phys* 82(4):3045–3067.
8. Qi XL, Zhang SC (2011) Topological insulators and superconductors. *Rev Mod Phys* 83(4):1057–1110.
9. Nielsen HB, Ninomiya M (1983) The Adler-Bell-Jackiw anomaly and Weyl fermions in a crystal. *Phys Lett B* 130(6):389–396.
10. Fukushima K, Kharzeev DE, Warringa HJ (2008) Chiral magnetic effect. *Phys Rev D* 78(7):074033.
11. Aji V (2012) Adler-Bell-Jackiw anomaly in Weyl semimetals: Application to pyrochlore iridates. *Phys Rev B* 85(24):241101.
12. Zyuzin AA, Wu S, Burkov AA (2012) Weyl semimetal with broken time reversal and inversion symmetries. *Phys Rev B* 85(16):165110.
13. Grushin AG (2012) Consequences of a condensed matter realization of Lorentz-violating QED in Weyl semi-metals. *Phys Rev D* 86(4):045001.
14. Zyuzin AA, Burkov AA (2012) Topological response in Weyl semimetals and the chiral anomaly. *Phys Rev B* 86(11):115133.
15. Hosur P, Qi X (2013) Recent developments in transport phenomena in Weyl semimetals. *Comp Rend Phys* 14(9-10):857.
16. Chang M-C, Yang M-C (2015) Chiral magnetic effect in a two-band lattice model of Weyl semimetal. *Phys Rev B* 91(11):115203.
17. Cho GY, Bardarson JH, Lu Y-M, Moore JE (2012) Superconductivity of doped Weyl semimetals: Finite momentum pairing and electronic analog of the ^{3}He-A phase. *Phys Rev B* 86(21):214514.
18. Ojanen T (2013) Helical Fermi arcs and surface states in time-reversal invariant Weyl semimetals. *Phys Rev B* 87(24):245112.
19. Ashby PEC, Carbotte JP (2013) Magneto-optical conductivity of Weyl semimetals. *Phys Rev B* 87(24):245131.
20. Potter AC, Kimchi I, Vishwanath A (2014) Quantum oscillations from surface Fermi arcs in Weyl and Dirac semimetals. *Nat Commun* 5:5161.
21. Parameswaran SA, Grover T, Abanin DA, Pesin DA, Vishwanath A (2014) Probing the chiral anomaly with nonlocal transport in three-dimensional topological semimetals. *Phys Rev X* 4(4):031035.
22. Panfilov I, Burkov AA, Pesin DA (2014) Density response in Weyl metals. *Phys Rev B* 89(24):245103.
23. Burkov AA, Balents L (2011) Weyl semimetal in a topological insulator multilayer. *Phys Rev Lett* 107(12):127205.
24. Xu G, Weng H, Wang Z, Dai X, Fang Z (2011) Chern semimetal and the quantized anomalous Hall effect in $HgCr_2Se_4$. *Phys Rev Lett* 107(18):186806.
25. Singh B, et al. (2012) Topological electronic structure and Weyl semimetal in the $TlBiSe_2$ class of semiconductors. *Phys Rev B* 86(11):115208.
26. Bulmash D, Liu C-X, Qi X-L (2014) Prediction of a Weyl semimetal in $Hg_{1-x-y}Cd_xMn_yTe$. *Phys Rev B* 89(8):081106.
27. Liu JP, Vanderbilt D (2014) Weyl semimetals from noncentrosymmetric topological insulators. *Phys Rev B* 90(15):155316.
28. Huang SM, et al. (2015) A Weyl Fermion semimetal with surface Fermi arcs in the transition metal monopnictide TaAs class. *Nat Commun* 6:7373.
29. Weng H, et al. (2015) Weyl semimetal phase in non-centrosymmetric transition metal monophosphides. *Phys Rev X* 5(1):011029.
30. Xu S-Y, et al. (2015) Discovery of a Weyl fermion semimetal and topological Fermi arcs. *Science* 349(6248):613–617.
31. Lv BQ, et al. (2015) Experimental discovery of Weyl semimetal TaAs. *Phys Rev X* 5(3):031013.
32. Xu S-Y, et al. (2015) Discovery of the Weyl semimetal state in niobium arsenide. *Nat Phys* 11(9):748–754.
33. Yang L, et al. (2015) Weyl semimetal in non-centrosymmetric compound TaAs. *Nat Phys* 11(9):728–732.
34. Xu N, et al. (2015) Observation of Weyl nodes and Fermi arcs in TaP. arXiv: 1507.03983v1.
35. Xu S-Y, et al. (2015) Experimental discovery of a topological Weyl semimetal state in TaP. *Sci Adv* 1(10):e1501092.
36. Perdew JP, Burke K, Ernzerhof M (1996) Generalized gradient approximation made simple. *Phys Rev Lett* 77(18):3865–3868.
37. Kripyakevich PI, Gladyshevskii EI (1966) The crystal structure of strontium disilicide. *Crystallography* 11:818.
38. Weng H, Ozaki T, Terakura K (2009) Revisiting magnetic coupling in transition-metal-benzene complexes with maximally localized Wannier functions. *Phys Rev B* 79(23):235118.
39. Pringle GE (1972) The structure of $SrSi_2$: A crystal of class O (432). *Acta Crystallogr B* 28:2326.
40. Evers J (1978) Transformation of three-dimensional three-connected silicon nets in $SrSi_2$. *J Solid State Chem* 24(2):199.
41. Jian S-K, Yao H (2015) Correlated double-Weyl semimetals with Coulomb interactions: Possible applications to $HgCr_2Se_4$ and $SrSi_2$. *Phys Rev B* 92(4):045121.
42. Moon E-G, Xu C, Kim YB, Balents L (2013) Non-Fermi-liquid and topological states with strong spin-orbit coupling. *Phys Rev Lett* 111(20):206401.
43. Herbut IF, Janssen L (2014) Topological Mott insulator in three-dimensional systems with quadratic band touching. *Phys Rev Lett* 113(10):106401.
44. Fang C, Gilbert MJ, Dai X, Bernevig BA (2012) Multi-Weyl topological semimetals stabilized by point group symmetry. *Phys Rev Lett* 108(26):266802.
45. Xia Y, et al. (2009) Observation of a large-gap topological-insulator class with a single Dirac cone on the surface. *Nat Phys* 5(6):398.
46. Evers J, Weiss A (1974) Electrical properties of alkaline earth disilicides and digermanides. *Mater Res Bull* 9(5):549.
47. Lue CS (2013) Enhancement of thermoelectric performance driven by Ge substitution in $SrSi_2$ alloy. *J Phys D Appl Phys* 46(31):315303.
48. Wang Z, et al. (2013) Three-dimensional Dirac semimetal and quantum transport in Cd_3As_2. *Phys Rev B* 88(12):125427.
49. Neupane M, et al. (2014) Observation of a topological 3D Dirac semimetal phase in high-mobility Cd_3As_2. *Nat Commun* 5:3786.
50. Borisenko S, et al. (2014) Experimental realization of a three-dimensional Dirac semimetal. *Phys Rev Lett* 113(2):027603.
51. Liu ZK, et al. (2014) A stable three-dimensional topological Dirac semimetal Cd_3As_2. *Nat Mater* 13(7):677–681.
52. Liang T, et al. (2015) Ultrahigh mobility and giant magnetoresistance in the Dirac semimetal Cd_3As_2. *Nat Mater* 14(3):280–284.
53. Zdanowicz L (1967) Some optical properties of thin evaporated Cd_3As_2 films. *Phys Status Solidi* 20(2):473.
54. Sexer N (1967) Effets galvanomagnétiques et thermomagnétiques classiques dans l'arséniure de cadmium. *Phys Status Solidi* 21:225.
55. Aubin N, Caron LG, Jay-Gerin JP (1977) Band structure of cadmium arsenide at room temperature. *Phys Rev B* 15(8):3872.
56. Caron LG, Jay-Gerin JP, Aubin N (1977) Energy-band structure of Cd_3As_2 at low temperatures and the dependence of the direct gap on temperature and pressure. *Phys Rev B* 15(8):3879.
57. Wang Z, et al. (2012) Dirac semimetal and topological phase transitions in A_3Bi (A = Na, K, Rb). *Phys Rev B* 85(19):195320.
58. Liu ZK, et al. (2014) Discovery of a three-dimensional topological Dirac semimetal, Na_3Bi. *Science* 343(6173):864–867.
59. Xu SY, et al. (2015) Observation of Fermi arc surface states in a topological metal. *Science* 347(6219):294–298.
60. Bernevig BA, Hughes TL, Zhang SC (2006) Quantum spin Hall effect and topological phase transition in HgTe quantum wells. *Science* 314(5806):1757–1761.
61. Tegze M, Hafner J (1992) Electronic structure of alkali-pnictide compounds. *J Phys Condens Matter* 4(10):2449.
62. Scott MW (1969) Energy gap in $Hg_{1-x}Cd_xTe$ by optical absorption. *J Appl Phys* 40(10):4077.

63. Finkman E, Nemirovsky Y (1969) Infrared optical absorption of $Hg_{1-x}Cd_xTe$. *J Appl Phys* 50(6):4356.
64. Vidal J, et al. (2011) False-positive and false-negative assignments of topological insulators in density functional theory and hybrids. *Phys Rev B* 84(4):041109.
65. Aguilera I, et al. (2013) GW study of topological insulators Bi_2Se_3, Bi_2Te_3, and Sb_2Te_3: Beyond the perturbative one-shot approach. *Phys Rev B* 88(4):045206.
66. Heyd J, Scuseria GE, Ernzerhof M (2003) Hybrid functionals based on a screened Coulomb potential. *J Chem Phys* 118(18):8207.